Research Square

Preprints are preliminary reports that have not undergone peer review.
They should not be considered conclusive, used to inform clinical practice,
or referenced by the media as validated information.

Microstructure, Properties and Corrosion Resistance of As-Cast Al-12Si-1.0Mn-0.6Mg-xSc Alloys

Weiwei Yang
Central South University
Richu Wang
Central South University
Chaoqun Peng
Central South University
Zhiyong Cai (zycaimse@163.com)
Central South University https://orcid.org/0000-0002-4926-8441
Fanghe Guo
Central South University
Zichen Zhang
Central South University

Research Article

Keywords: Al-12Si alloy, Mechanical property, Thermo-physical property, Corrosion

Posted Date: March 15th, 2021

DOI: https://doi.org/10.21203/rs.3.rs-288534/v1

License: This work is licensed under a Creative Commons Attribution 4.0 International License.
Read Full License

Abstract

Al-12Si-1.0Mn-0.6Mg-*x*Sc (*x* = 0, 0.1, 0.2, and 0.3) alloys for electronic packaging were prepared by ingot metallurgy, and the microstructure, mechanical properties, thermo-physical properties and corrosion resistance were compared. A fine and dispersed Al_3Sc phase is observed and the acicular β-Fe phase transforms into a Chinese character or massive α-Fe phase in the alloys with Sc addition. When the Sc content increases from 0 to 0.3%, the secondary dendritic arm spacing and the size of the eutectic Si reduce from 17.9 μm and 5.3 μm to 12.8 μm and 3.1 μm, respectively. Simultaneously, the morphology of eutectic Si changes from a rough long rod to an ellipsoid. The thermal expansion coefficient and thermal conductivity of the alloys reduce slightly with increasing the Sc content. The flexural strength of 291.9 MPa is obtained for the Al-12Si-1.0Mn-0.6Mg-0.3Sc, an increment of 20.4% as compared with the Sc-free alloy. Furthermore, the corrosion resistance of the alloys is improved by the minor Sc addition.

1. Introduction

With the development of electronica, advanced electronic packaging materials with excellent comprehensive properties are demanded, such as low density and coefficient of thermal expansion (CTE), high electrical and thermal conductivity, and excellent corrosion resistance. Based on these requirements, Al-based electronic packaging material has been the fastest developing one. Recently, Al-Si alloys have the advantages of lightweight, high thermal conductivity, good wear resistance, high specific strength, and have been applied in aerospace and other space technology fields [1-3]. Compared with Al-SiCp composites, Al-Si alloys have better machinability and are suitable for precision machined parts [4,5]. With the increase of Si content, the density and linear expansion coefficient of high silicon alloy decrease, but the bulk polygonal primary Si phase is formed in the alloy, which reduces the processing and mechanical properties of the alloy. Among which Al-12Si eutectic alloys have excellent machining performance, laser weldability, and corrosion resistance, it is suitable for the application of cover material in electronic packaging. However, the binary Al-12Si alloy presents low strength due to the large-sized Si phases and low solid solubility of Si in Al (0.05 at.% at room temperature), as well as lack of strengthening phase.

Micro-alloying is a feasible method to improve the strength of Al-12Si alloy. Generally, Cu and Mg elements are added in the traditional Al-Si alloys [6]. The addition of Mg forms fine Mg_2Si precipitate after heat treatment, and then enhances the mechanical properties of the alloys [7]. The addition of Cu forms Al_2Cu phase, which also improves the strength of the alloys [8,9], but significantly reduces the corrosion resistance [10]. Therefore, the combined addition of Mg and Mn is selected instead of Mg and Cu. The addition of Mn is helpful for refining the grains, homogenizing the microstructure, and improving the strength of the alloys. In Al-Si alloys, Mn mainly exists in the form of Al_6Mn. When Mn and Fe coexist in the alloys, a complex AlFeMnSi phase will be formed. Consequently, the addition of Mn can eliminate or reduce the harmful effect of Fe in Al alloys [11,12]. In addition, Mn neutralizes the impurity iron in the as-cast alloy, so that the thick needle phase is transformed into a smoother block or short bar phase, which

makes the Fe containing phase evenly distributed and reduces the potential difference, thus improving the corrosion resistance of the alloy. Qiu et al. [13] found that adding Mn to Al-7Si-Mg alloy could promote the transformation of morphology of iron intermetallic. With the increase of Mn content, α-Al(Mn,Fe)Si finally transforms from branched shape to Chinese script shape，which usually occurs when Mn and Fe have an appropriate ratio.

Among the trace alloying elements, Sc is an excellent grain refiner and strengthening element in Al alloys [14-16]. The Sc-containing Al alloys form Al_3Sc precipitates at the nanometer scale in the grains [17-19]. Pandee et al. [20] found that minor Sc addition refined eutectic Si in the as-cast Al-7Si-0.3Mg alloys. Tzeng et al. [21,22] reported that in the Al-11.6Si alloys, the Sc addition changed the needle Fe-bearing phase into massive-like. Furthermore, the formed Al_3Sc particles could effectively restrain grain growth and hinder dislocation movement, and then improve the strength of the alloys. Pramod et al. [23] found that when 0.4 wt.% Sc is added to A356 alloy, the secondary dendritic arm spacing (SDAS) could be reduced by 50%. The Vickers hardness, tensile strength, yield strength and ductility of the alloy were increased by 20%, 25%, 20%, and 30%, respectively. The improved mechanical properties are ascribed to morphological evolution of eutectic Si from plate-like to fibrous and spherical by Sc addition. Xu et al. [24] found that when 1.5 wt.% Cu and 0.6 wt.% Sc are added to A356 alloy, it has the best tensile properties, with tensile strength, yield strength and elongation of 349.7 MPa, 236.9 MPa and 14.6%. The addition of Sc can transform the tabular eutectic Si into fibrous, promote the precipitation of θ'-Al_2Cu and Al_3Sc, and improve the tensile properties of the alloy.

To further improve the mechanical properties of Al-12Si alloys and maintain their good thermo-physical properties and corrosion resistance, the present work investigated the effects of different contents of Sc (0, 0.1%, 0.2%, and 0.3%) on the microstructure, mechanical properties, thermo-physical properties, and corrosion resistance of Al-12Si-1.0Mn-0.6Mg alloys prepared by ingot metallurgy.

2. Experimental Process

Four experimental alloys were prepared by graphite crucible melting in a resistance furnace at 760 ℃. Raw materials of 99.95% pure Al (weight percent unless otherwise specified), 99.9% pure Mg, Al-30%Si, Al-13%Mn, and Al-2%Sc master alloys were used. When all the above materials were completely melted and the temperature was stable, 99.9% pure Mg was pressed gently into the melt, then stirred and held for approximately 15 minutes. Subsequently, the alloys were degassed and poured into the metal mold for cooling. The as-cast Al-12Si-1.0Mn-0.6Mg-*x*Sc alloys were homogenized at 520 ℃ for 12 h to eliminate dendrite segregation during casting and reduce ingots heterogeneity. Table 1 shows the chemical composition of the Al-12Si-1.0Mn-0.6Mg-*x*Sc (*x* = 0, 0.1, 0.2, and 0.3) alloys, which was determined by inductively coupled plasma atomic emission spectrometry (ICP-AES).

Table 1 Chemical composition of the Al-12Si-1.0Mn-0.6Mg-*x*Sc alloys (wt.%)

Alloy	Si	Mn	Mg	Sc	Fe	Al
Al-12Si-1.0Mn-0.6Mg	11.94	1.03	0.60	–	0.13	Bal.
Al-12Si-1.0Mn-0.6Mg-0.1Sc	11.93	1.08	0.60	0.10	0.13	Bal.
Al-12Si-1.0Mn-0.6Mg-0.2Sc	12.01	1.04	0.59	0.19	0.14	Bal.
Al-12Si-1.0Mn-0.6Mg-0.3Sc	12.02	1.06	0.59	0.30	0.14	Bal.

Optical microscope (OM, Leica DMI 300M, Germany) was used to observe the microstructure of the alloys, and ImageJ software was used to measure the size of eutectic Si and SDAS. X-ray diffraction (XRD, D/MAX 2550, Japan) was used to analyze the phase composition of the alloys. The scanning speed was 4 (°)/min and the scanning range was 10°-90°. Scanning electron microscope (SEM, Quanta 200, Holland) was used to observe the microstructural evolution and fracture morphologies. The alloys were mechanically ground, polished, and etched for 20 s with Keller's reagent (1%HF - 1.5%HCl - 2.5%HNO_3 - 95%H_2O, volume fraction). The electron probe microanalyzer (EPMA, JAX-8230, Japan) was used for qualitative analysis of the composition of the alloy microregions.

A thermo-mechanical tester (NETZSCH DIL 402 PC, Germany) was used to test the coefficients of thermal expansion of the alloys at 25-300 ℃. The dimension of the alloy samples was 5 mm × 5 mm × 25 mm. Thermal diffusivity and specific heat were measured using laser flash and calorimetric methods (NETZSCH LFA427/3/G, German), respectively. The thermal conductivity of the alloys was obtained by calculation. The dimension of the alloy samples was Φ12.6 mm × 3 mm. The density of the alloys was determined by the Archimedes drainage method. The hardness of the alloys was tested using a Vickers hardness tester with a loading time of 30 s and a loading of 0.98 kN. An electronic universal material testing machine (Instron MTS850, USA) was used for tensile and bending experiments at room temperature with a loading speed of 0.2 mm/min. The tensile samples were manufactured in dumbbell shape according to international standards. The bending sample size was 3 mm × 10 mm ×50 mm. Three samples were taken in each state and the measurement results were averaged. The electrochemical corrosion of the four alloys was carried out, and the corrosion resistance of the alloys was observed through the changes of the dynamic potential polarization curves. The dynamic potential polarization curves were tested on an electrochemical workstation (IM6ex) with a scanning speed of 1 mV/s and a scanning voltage range of -1.2 to -0.3 V.

3. Results And Discussion

3.1 Microstructural characteristics

Fig. 1 shows the optical micrographs of the as-cast Al-12Si-1.0Mn-0.6Mg-*x*Sc alloys. It is observed from Fig. 1a and b that there are a large number of dendrites in the Al-12Si-1.0Mn-0.6Mg alloy, which are mainly composed of white α-Al and dark gray eutectic Si. With the addition of Sc, the morphology of eutectic Si changes from rough long rod to ellipsoid, and distributes uniformly in the α-Al matrix, as seen

from Fig. 1c to h. The α-Al dendrites are refined obviously, which is ascribed to the formation of Al_3Sc particles in the matrix. The Al_3Sc phase is coherent with the matrix with a lattice mismatch of only 1.5%, which provides more heterogeneous nucleation sites for nucleation and refines crystal grains. In addition, it is observed that the irregular coarse phase precipitated on the α-Al dendrite boundary. With the increase of Sc content, the long needle-like phase gradually decreases and transforms into an irregular bone-like or Chinese character-like phase.

Fig. 2 shows the size of eutectic Si and SDAS in the Al-12Si-1.0Mn-0.6Mg-*x*Sc alloys. It is seen that the size of eutectic Si is reduced from 3.1 μm in the Al-12Si-1.0Mn-0.6Mg-0.3Sc alloy, a reduction of 41.5% compared with that of the Sc-free alloy. At the same time, SDAS decreases from 17.9 μm to 12.8 μm, decreasing by 28.5%.

Fig. 3 shows the XRD patterns of the Al-12Si-1.0Mn-0.6Mg-*x*Sc alloys. It can be seen that the main constituent phases in the alloys are α-Al and eutectic Si phase. No other corresponding diffraction peaks are observed in the diffraction spectrum due to their low volume fraction.

The SEM-BSD micrographs of the as-cast Al-12Si-1.0Mn-0.6Mg-*x*Sc alloys are shown in Fig. 4. It is seen that the morphology of the white phase in the alloys gradually changes from the needle-like phase to the bone-like phase and then into the Chinese character-like or massive phase with increasing Sc content. When the Sc content increases from 0.2 wt.% to 0.3 wt.%, the size of the white massive phase decreases from 100 μm to 40 μm, and the distribution becomes more uniformly.

SEM-EDS was used to detect the second phase in the Al-12Si-1.0Mn-0.6Mg and Al-12Si-1.0Mn-0.6Mg-0.3Sc alloys, and the results are exhibited in Fig. 5. As seen from Fig. 5a, the irregular white phase contains elements of Al, Si, Fe and Mn, which should be Al(Fe, Mn)Si phase. According to Ref. [25], the needle-like phase in the Al-12Si-1.0Mn-0.6Mg alloy is β-Al_5(Fe, Mn)Si. When 0.3% Sc is added, the precipitated bulk phase is α-Al(Fe, Mn)Si in Fig. 5b. The acicular β-Fe phase tends to cause stress concentration to split the matrix and reduce the mechanical properties of the alloy. The addition of Sc transforms the acicular β-Fe phase into Chinese character or massive α-Fe phase, reducing the adverse effects and improving the mechanical properties of the alloys. When 0.3% Sc is added, the amount of the massive α-Fe phase remains unchanged, the size is reduced and the distribution is uniform, which further improves the overall performance of the alloy.

It can be seen from the SEM-EDS energy spectrum analysis results of the alloy in Fig. 6 that there are light gray round phases and fine bright white phases distributed in the alloy matrix. According to the results of EDS, the atomic ratio of combined Al and Sc in Fig. 6a is close to 3:1, and it is determined that the fine bright white phase is Al_3Sc. In Fig. 6(b), the atomic ratio of combined Mg to Si is close to 2:1, and the light gray round phase is determined to be Mg_2Si.

Fig. 7 shows the EPMA element distribution diagram of Al-12Si-1.0Mn-0.6Mg-0.3Sc alloy, and the element distribution is shown in different colors. It can be seen that Si is mainly distributed in the eutectic region,

but Fe and Mn are mainly distributed in the irregular white phase. This phenomenon indicates that the Fe element in the alloy is dissolved in the Mn-rich phase and forms α-Al(FeMn)Si phase in the alloy. Additionally, Mg and Sc elements are precipitated in the form of the second phase Mg_2Si and Al_3Sc in the alloy.

3.2 Thermo-physical properties

The density of the Al-12Si-1.0Mn-0.6Mg-*x*Sc alloys is listed in Table 2. It can be observed from the table that with the addition of Sc, the measured density of the alloys becomes closer to the theoretical density. The densification reaches 99.8% when 0.3% Sc is added.

The main factors affecting the thermal expansion coefficient of Al-Si alloys are the thermal expansion properties of alloy components and the restraint of interface between the substrate and the reinforcement. The thermal expansion coefficient of Al is 23.6×10^{-6}/K, while that of Si is 4.1×10^{-6}/K. Therefore, the low thermal expansion property of Al-Si alloys mainly depends on Si element. The size of Si particles has a certain effect on the thermal expansion performance of Al-Si alloys. As the size of Si particles decreases, the thermal expansion coefficient of the alloy decreases [26]. This is because the large-sized particles in the Al matrix are easy to aggregate and thus generate greater stress. In the subsequent process, larger strain will be generated, resulting in the increase of the thermal expansion coefficient of the alloys [27,28].

Table 2 Density of the Al-12Si-1.0Mn-0.6Mg-*x*Sc (*x* = 0, 0.1, 0.2, and 0.3) alloys

Material	Measured density (g/cm^3)	Theoretical density (g/cm^3)	Relative Density (%)
Al-12Si-1.0Mn-0.6Mg	2.667	2.699	98.8
Al-12Si-1.0Mn-0.6Mg-0.1Sc	2.672	2.700	98.9
Al-12Si-1.0Mn-0.6Mg-0.2Sc	2.683	2.700	99.4
Al-12Si-1.0Mn-0.6Mg-0.3Sc	2.696	2.701	99.8

The relationship between thermal expansion coefficient and temperature of the Al-12Si-1.0Mn-0.6Mg-*x*Sc (*x* = 0, 0.1, 0.2, and 0.3) alloys is shown in Fig. 8. It can be seen that the thermal expansion coefficient of the alloys increases with increasing the temperature. The variation range of thermal expansion coefficient of the alloys at low temperature is larger than that at high temperature. This phenomenon can be explained by the linear mixing law, the rule of mixture (ROM) model [29].

$$\alpha_c = \alpha_m V_m + \alpha_p V_p \quad (1)$$

Where α is the linear thermal expansion coefficient, V is the volume fraction, subscript c is the composite material, subscript m and p are the matrix and reinforcement particles of the composite material, respectively.

According to the ROM law, the mixed thermal expansion coefficient of the alloy was calculated, in which the thermal expansion coefficient of Mg, Mn and Sc at room temperature was 26×10^{-6}/K, 23×10^{-6}/K, and 10.2×10^{-6}/K, respectively. Therefore, the mixed thermal expansion coefficients of the four alloys are calculated as 25.2×10^{-6}/K, 24.2×10^{-6}/K, 23.3×10^{-6}/K, and 22.6×10^{-6}/K. The coefficient of thermal expansion in the low temperature range is smaller than the average coefficient of thermal expansion of the mixture. When the temperature rises to 300 ℃, the alloy with 0.3 wt.% Sc element approaches the average thermal expansion coefficient of the mixture, and the difference in thermal expansion coefficients of the four alloys decreases obviously.

The addition of Sc element can significantly affect the thermal expansion coefficient of alloys. On the one hand, the thermal expansion coefficient of the alloys is affected by the size of the reinforcement, and the smaller size of the reinforcement usually reduces the thermal expansion coefficient of the alloys. Among these alloys, the Mn-contained phase size is the smallest in the alloy added 0.3% Sc. On the other hand, with the addition of Sc element, the alloys precipitate a fine and uniform Al_3Sc phase, resulting in an enhanced interfacial bonding in alloys, which hinders the expansion behavior of the matrix, and reducing the thermal expansion coefficient.

The thermal conductivity of the as-cast Al-12Si-1.0Mn-0.6Mg-xSc alloys is listed in Table 3. The thermal conductivity of the alloys at room temperature decreases after the addition of trace element Sc. The thermal conductivity of the Al-12Si-1.0Mn-0.6Mg-0.3Sc alloy is reduced from 152.2 W/(m•K) to 142.7 W/(m•K), a reduction of 6.2% compared with the Sc-free alloy.

Table 3 Thermal conductivity and thermal expansion coefficient of the Al-12Si-1.0Mn-0.6Mg-xSc (x = 0, 0.1, 0.2, and 0.3) alloys

Material	Thermal conductivity[W/(m•K)]	Coefficient of thermal expansion ($\times10^{-6}$/K)			
		100℃	200℃	300℃	400℃
Al-12Si-1.0Mn-0.6Mg	152.2	19.6	21. 8	22.7	23.3
Al-12Si-1.0Mn-0.6Mg-0.1Sc	140.3	18.0	20.6	22.6	23.3
Al-12Si-1.0Mn-0.6Mg-0.2Sc	142.5	18.6	21.2	22.6	23.2
Al-12Si-1.0Mn-0.6Mg-0.3Sc	142.7	18.7	21.4	22.5	23.1

Thermal conduction of Al-Si alloys mainly depends on the combined effect of free electrons in the Al matrix and phonons in the Si phase. The main factors affecting the thermal conductivity of Al-Si alloys are the shape and size distribution of the Si phase, the density of the material, the second phase [30]. In addition, the alloy interface and lattice distortion also make a big difference in the thermal conductivity. In the process of heat conduction, there exists some interfacial thermal resistance, and the interfacial resistance of alloys will hinder the movement of electrons and phonons, thus reducing the thermal conductivity of the materials. If the interface bonding between the reinforcing phase and the matrix reaches an ideal state, the interface thermal resistance is zero. However, in fact, due to the difference in physical and chemical properties between the reinforcing phase and the matrix, the interface bonding cannot reach the ideal state. However, increasing the content of Si particles or decreasing the size of Si particles will lead to the increase of alloy interface, resulting in the increase of interface thermal resistance and the decrease of thermal conductivity of Al-Si alloys [31,32].

3.3 Mechanical properties

Fig. 9 shows the typical stress-strain curves of the Al-12Si-1.0Mn-0.6Mg-*x*Sc alloys. Table 4 lists the mechanical properties of the four alloys. After adding Sc element, the mechanical properties of the alloys are improved. Among these alloys, the Al-12Si-1.0Mn-0.6Mg-0.3Sc alloy obtains the optimal mechanical properties. Compared with the Sc-free alloy, the flexural strength of the alloy is increased from 242.5 MPa to 291.9 MPa, an increment of 20.4%. Furthermore, the tensile strength, elongation and hardness of the alloy are also increased by 20.7%, 109.1% and 3.4%, respectively. The hardness increment can be ascribed to the grain refinement of alloys with Sc addition. While the enhanced strength is the combined effect of grain refinement strengthening and precipitation strengthening. The fine Al_3Sc phase precipitated from the alloys increases the recrystallization temperature and hinders the dislocation movement, and then enhances the strength of the alloys.

Table 4 Mechanical properties of the Al-12Si-1.0Mn-0.6Mg-*x*Sc (*x* = 0, 0.1, 0.2, and 0.3) alloys

Material	Bending strength (MPa)	Tensile strength (MPa)	Elongation (%)	Microhardness (HV)
Al-12Si-1.0Mn-0.6Mg	242.5	137.4	2.2	59.4
Al-12Si-1.0Mn-0.6Mg-0.1Sc	270.9	151.1	3.6	60.7
Al-12Si-1.0Mn-0.6Mg-0.2Sc	286.4	163.8	4.4	61.3
Al-12Si-1.0Mn-0.6Mg-0.3Sc	291.9	165.9	4.6	61.4

Fig. 10 shows the tensile fracture morphologies of the Al-12Si-1.0Mn-0.6Mg-*x*Sc alloys. As can be seen from Fig. 10(a) and (b), the fracture surface of the Al-12Si-1.0Mn-0.6Mg alloy sample appears a large

number of quasi-cleavage planes, which belongs to brittle fracture. After the addition of Sc, dimples can be observed on the surface of the fractured samples. With the increase of Sc content, the number of dimples increases and the distribution becomes more uniform. In the fractured surface of the Al-12Si-1.0Mn-0.6Mg-0.1Sc alloy, there are tearing edges with different sizes near the dimples, and the fracture mode changes from brittle fracture to mixed fracture mode of brittle fracture and ductile fracture. Furthermore, the number of dimples on the fracture surface is the largest and distributed uniformly in the Al-12Si-1.0Mn-0.6Mg-0.3Sc alloy. Therefore, the addition of Sc not only improve the strength of Al-12Si-1.0Mn-0.6Mg alloy but also the plasticity.

Fig. 11 shows the shrinkage cavity on the fracture surface of the Al-12Si-1.0Mn-0.6Mg alloy. A large number of aciculate β-Fe phase is observed. The aciculate β-Fe phase generally distributes at the solid-liquid phase interface, which hinders the flow of the alloy liquid phase and cannot be supplied quickly, resulting in a large number of shrinkage holes. When the alloy is subjected to stress, the stress concentration around the shrinkage cavity occurs, and the microcrack continuously expands, and finally the alloy will break. After the addition of Sc, the needle β-Fe phase in the alloys transforms into the Chinese character α-Fe phase or the massive α-Fe phase, which improves the fluidity and the mechanical properties of the alloys.

3.4 Corrosion resistance

The dynamic potential polarization curves of the Al-12Si-1.0Mn-0.6Mg-*x*Sc alloys are shown in Fig. 12. It is seen that there is no inflection point on the polarization curve of the Al-12Si-1.0Mn-0.6Mg alloy, indicating that it has no pseudo passivation phenomenon, and pitting corrosion begins directly after reaching the corrosion potential. An inflection point appears on the polarization curve of the Sc-containing alloys, indicating that these alloys have passivation during the corrosion process. After reaching the corrosion potential, the corrosion products of the alloy adhere to the alloy matrix and form a certain passivation film. As the reaction progresses, the passivation film ruptures and pitting of the alloy begins to appear.

It can be seen from the self-corrosion potential and corrosion current density of the four alloys in Table 5 that the corrosion current density and self-corrosion potential of the Al-12Si-1.0Mn-0.6Mg alloy are 5.59×10^{-6} A/cm^2 and -0.76 V, respectively. With increasing the Sc content, the corrosion current density of the alloys decreases and the self-corrosion potential shifts negatively. The corrosion current density and self-corrosion potential of the 0.3Sc-containing alloy are 2.26×10^{-6} A/cm^2 and -0.86 V, respectively. Compared with the 0.1Sc-containing alloy, the corrosion current density increases slightly and the corrosion resistance decreases. But the overall corrosion resistance of the alloys with the addition of Sc is improved compared to the Sc-free alloy. On the one hand, the addition of Sc reduces the corrosion resistance of Al-12Si alloy to a certain extent. After adding trace alloying elements, more compounds are precipitated in the alloys, which increase the potential difference among the phases in the alloys. Consequently, the chemical stability and corrosion resistance of the alloys are reduced. On the other hand, the addition of Sc changes the morphology of eutectic Si in the alloys, and makes the distribution

of intermetallic compounds more uniform, then improves the corrosion resistance of the Al-12Si-1.0Mn-0.6Mg-*x*Sc alloys.

Table 5 Self-corrosion potential and corrosion current density of the Al-12Si-1.0Mn-0.6Mg-*x*Sc (*x* = 0, 0.1, 0.2, and 0.3) alloys

Material	E_{corr} (V)	I_{corr} (A/cm^2)
Al-12Si-1.0Mn-0.6Mg	-0.76	5.59×10^{-6}
Al-12Si-1.0Mn-0.6Mg-0.1Sc	-0.80	1.53×10^{-6}
Al-12Si-1.0Mn-0.6Mg-0.2Sc	-0.83	2.04×10^{-6}
Al-12Si-1.0Mn-0.6Mg-0.3Sc	-0.86	2.26×10^{-6}

4. Conclusions

(1) With the addition of Sc, a fine and dispersed Al_3Sc phase is observed, and the acicular β-Fe phase transforms into a Chinese character or massive α-Fe phase. When the Sc content increases from 0 to 0.3%, the secondary dendritic arm spacing (SDAS) and the size of eutectic Si reduce from 17.9 μm and 5.3 μm to 12.8 μm and 3.1 μm, a reduction of 28.8% and 41.5%, respectively. The morphology of eutectic Si changes from rough long rod to ellipsoid, and distributes uniformly in the matrix.

(2) Compared with the Sc-free alloy, the thermal conductivity and thermal expansion coefficient of the Al-12Si-1.0Mn-0.6Mg-0.3Sc alloy decreases from 152.2 W/(m•K) and 19.6×10^{-6} /K to 142.7 W/(m•K) and 18.7×10^{-6} /K, respectively.

(3) The flexural strength, tensile strength, elongation and hardness of the Al-12Si-1.0Mn-0.6Mg-0.3Sc alloy reach the maximum values of 291.9 MPa, 165.9 MPa, 4.6% and 61.4 HV, respectively. The fracture mode is a combination of brittle fracture and ductile fracture.

(4) Compared with the Sc-free alloy, the corrosion resistance of the alloys with the addition of Sc is improved. The corrosion current density and self-corrosion potential of the Al-12Si-1.0Mn-0.6Mg-0.3Sc alloy are 2.26×10^{-6} A/cm^2 and -0.86 V, respectively.

Declarations

Acknowledgement

The authors are grateful for the financial support provided by the National Nature Science Foundation of China (51804349), the China Postdoctoral Science Foundation (2018M632986), and the Department of Science and Technology of Hunan Province (2019JJ50766, 2020GK2044).

References

1. X. T. Qu, L. Zhang, M. Wu, S.B. Ren, Prog. Nat. Sci. **21**(3), 189–197 (2010)
2. N. Kang, P. Coddet, C.Y. Chen, Y. Wang, H. Liao, C. Coddet, Mater. Des. **99**, 120–126 (2016)
3. W. L. Zhang, D.Y. Ding, P. Gao, Mater. Des. **90**, 834–838 (2016)
4. W. Yu, J. K. Yu, Mater. Chem. Phys. **139**, 783–788 (2013)
5. Z. Cai, R. Wang, C. Zhang, C. Peng, L. Wang, J. Mater. Sci. Mater. Electron. **26**, 4234–4240 (2015)
6. C. T. Wu, S.L. Lee, M.H. Hsieh, J.C. Lin, Metall. Mater. Trans. A. **61**(3), 1074–1079 (2010)
7. M. Yildirim, D. Oezyuerek, Mater. Des. **51**, 767–774 (2013)
8. S. Beroual, Z. Boumerzoug, P. Paillard, Y. Borjon-Piron, J. Alloys Compd. **784**, 1026–1035 (2019)
9. F. H. Guo, R.C. Wang, C.Q. Peng, Z.Y. Cai, Y.X. Liu, Y. Feng, X.F. Wang, J. Mater. Sci. Mater. Electron. **31**, 5416–5424 (2020)
10. F. Grosselle, G. Timelli, F. Bonollo, Mater. Sci. Eng. A. **527**(15), 3536–3545 (2010)
11. S. X. Ji, W.C. Yang, F. Gao, D. Waston, Z.Y. Fan, Mater. Sci. Eng. A. **564**, 130–139 (2013)
12. C. Lin, S.S. Wu, S.L. Lü, P. An, L. Wan, Intermetallics. **32**, 176–183 (2013)
13. K. Qiu, R.C. Wang, C.Q. Peng, N.G. Wang, Z.Y. Cai, C. Zhang, Trans. Nonferrous Met. Soc. China. **25**(11), 3546–3552 (2015)
14. Y. K. Li, X.D. Du, Y. Zhang, Z. Zhang, J.W. Fu, S.A. Zhou, Y.C. Wu, Appl. Phys. A. **124**(2), 144 (2018)
15. M. S. Kaiser, M.R. Basher, A.S.W. Kurny, J. Mater. Eng. Perform. **21**(7), 1504–1508 (2012)
16. Y. C. Tzeng, C.T. Wu, S.L. Lee, Mater. Lett. **161**, 340–342 (2015)
17. K. Puparattanapong, C. Limmaneevichitr, Trans. Indian Inst. Met. **69**(8), 1587–1594 (2016)
18. C. Tzeng, C.T. Wu, C.H. Yang, S.L. Lee, Mater. Sci. Eng. A. **614**, 54–61 (2014)
19. C. Xu, W.L. Xiao, S.J. Hanada, H. Yamagata, Mater. Charact. **110**, 160–169 (2015)
20. P. Pandee, C. Gourlay, S.A. Belyakov, R. Ozaki, H. Yasuda, C. Limmaneevichitr, Metall. Mater. Trans. A. **45**(10), 4549–4560 (2014)
21. Y. C. Tzeng, C.T. Wu, M.L. Tsai, H.Y. Bora, J.L. Horng, Mater. Sci. Eng. A. **593**, 103-110 (2014)
22. Y. C. Tzeng, S.Y. Jian, Mater. Sci. Eng. A. **723**, 22–28 (2018)
23. S. L. Pramod, A.K.P. Rao, B.S. Murty, S.R. Bakshi, Mater. Sci. Eng. A. **674**, 438–450 (2016)
24. C. Xu, C. L. Ma, Y. F. Sun, S. Hanada, G. X. Lu, S. K. Guan, J. Alloys Compd. **810**, 151944 (2019)
25. X. J. Suo, H.C. Liao, Y.Y. Hu, U.S. Dixit, P. Petrov, J. Mater. Eng. Perform. **27**, 2910–2920 (2018)
26. Y. Y. Chen, D.D.L, Chung, J. Mater. Sci. **29**(23), 6069–6075 (1994)
27. X. W. Zhu, R.C. Wang, C.Q. Peng, W.S. Liu, J. Peng, J. Mater. Sci. Mater. Electron. **25**(11), 4889–4895 (2014)
28. Z. Y. Cai, C. Zhang, R.C. Wang, C.Q. Peng, K. Qiu, Y. Feng, Mater. Des. **87**, 996–1002 (2015)
29. N. Chawla, K. Chawla, Metal. Matrix. Compos, 2nd edn. (Springer, New York, 2013), pp. 37–54

30. Y. Zhang, J.W. Li, L.L. Zhao, H.L. Zhang, X.T. Wang, Mater. Des. **63**, 838-847 (2014)
31. S. Elomari, M.D. Skibo, A. Sundarrajan, H. Richards, Compos. Sci. Technol. **58**, 369–376 (1998)
32. D. P. H. Haselman, K. Y. Donaldson, A. L. Geiger, J. Mater. Sci. Lett. **12**(6), 420–423 (1993)

Figures

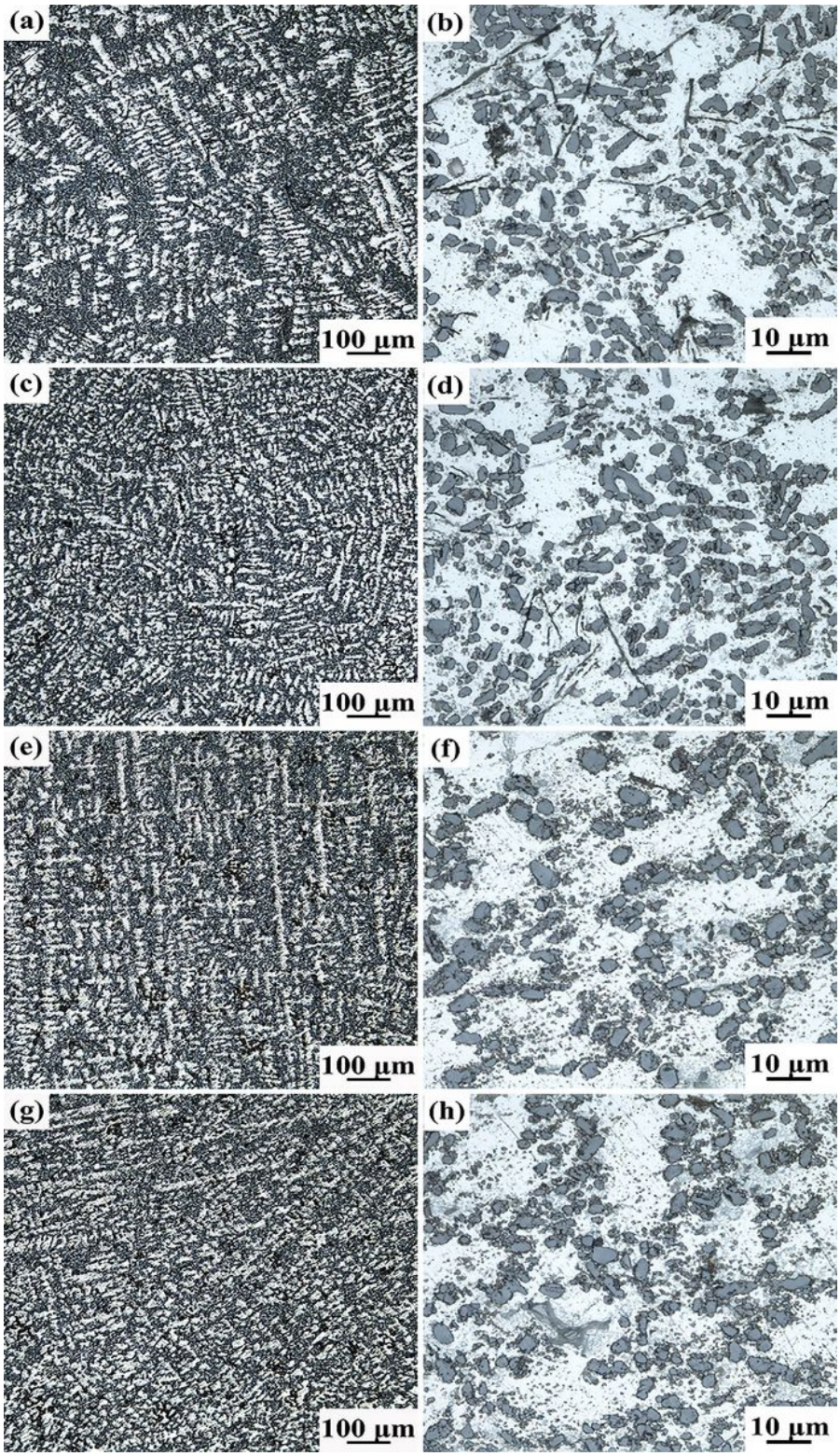

Figure 1

Optical micrographs of the as-cast Al-12Si-1.0Mn-0.6Mg-xSc (x = 0, 0.1, 0.2, and 0.3) alloys

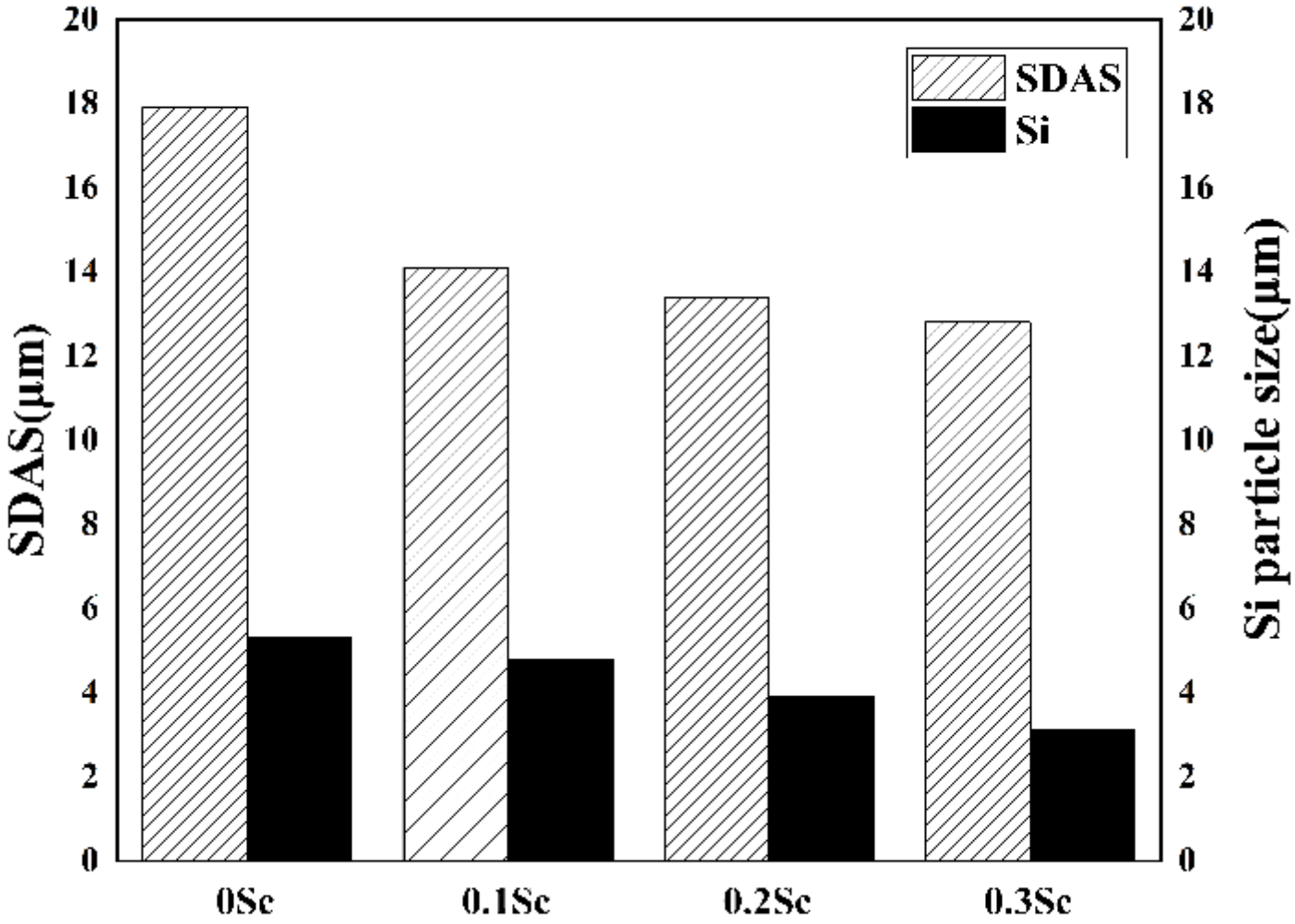

Figure 2

Quantitative metallographic analysis of the eutectic Si size and SDAS in the Al-12Si-1.0Mn-0.6Mg-xSc (x = 0, 0.1, 0.2, 0.3) alloys

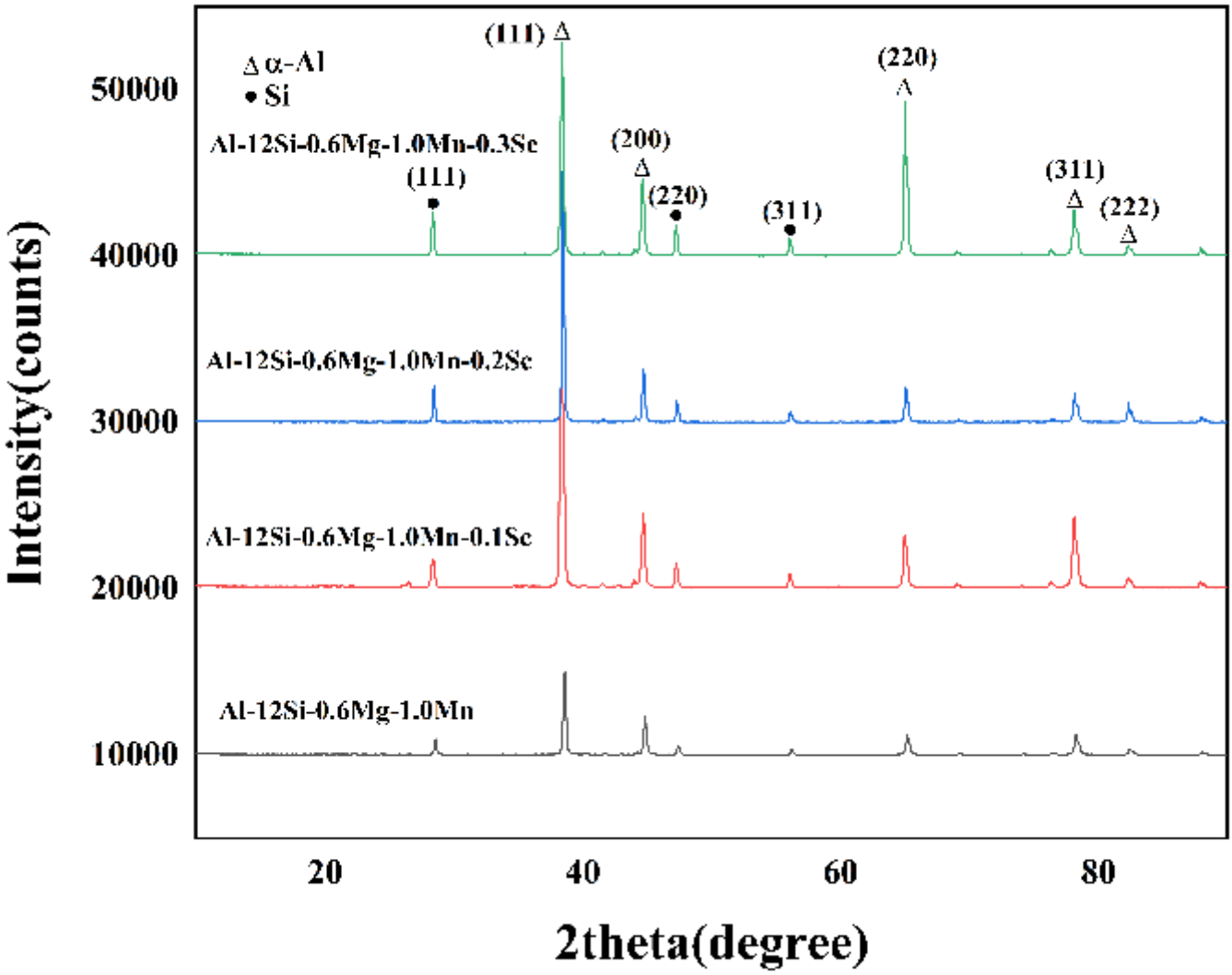

Figure 3

XRD patterns of the Al-12Si-1.0Mn-0.6Mg-xSc (x = 0, 0.1, 0.2, and 0.3) alloys

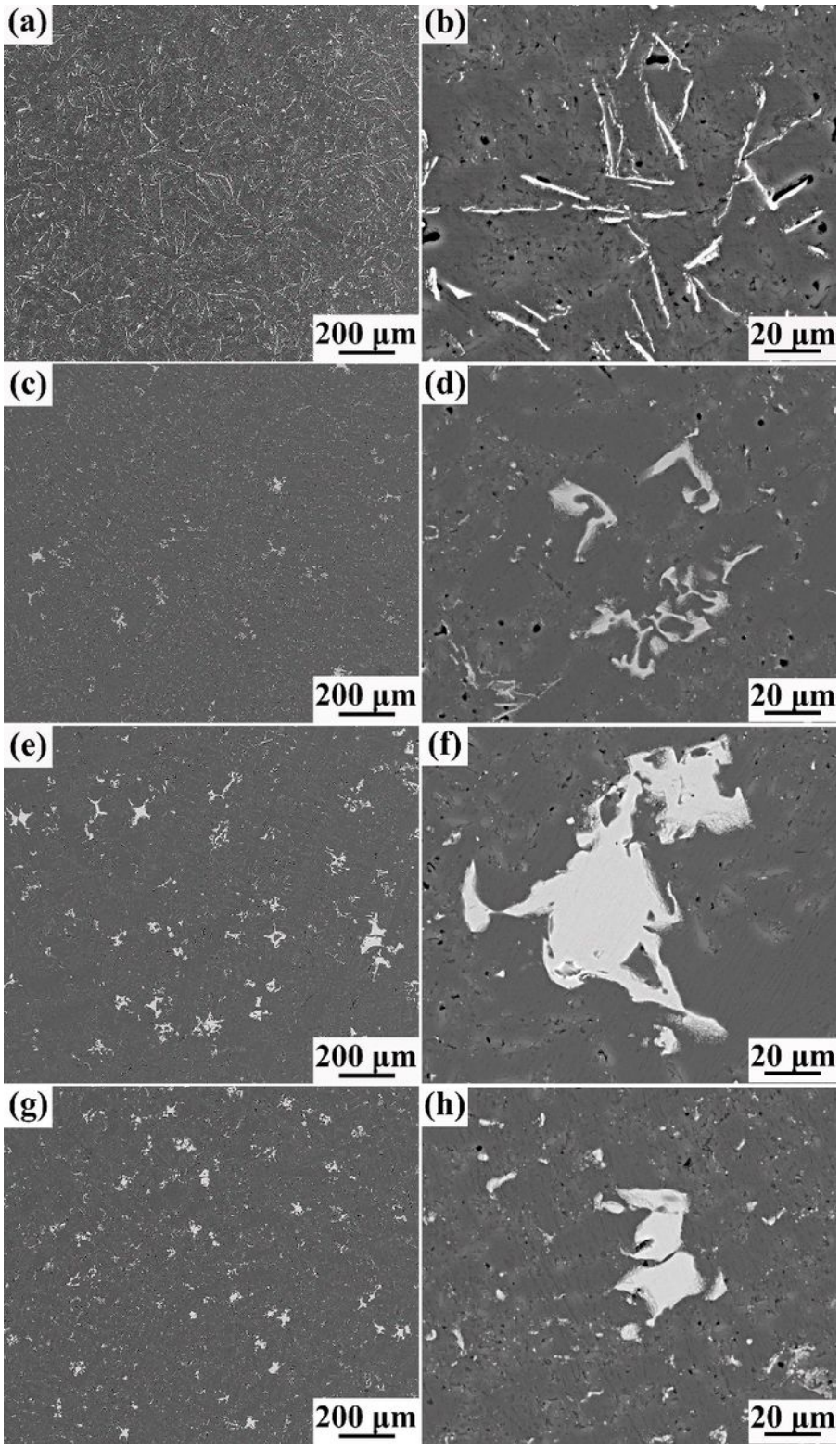

Figure 4

SEM-BSD micrographs of the Al-12Si-1.0Mn-0.6Mg-xSc (x = 0, 0.1, 0.2, and 0.3) alloys Note: The designations employed and the presentation of the material on this map do not imply the expression of any opinion whatsoever on the part of Research Square concerning the legal status of any country, territory, city or area or of its authorities, or concerning the delimitation of its frontiers or boundaries. This map has been provided by the authors.

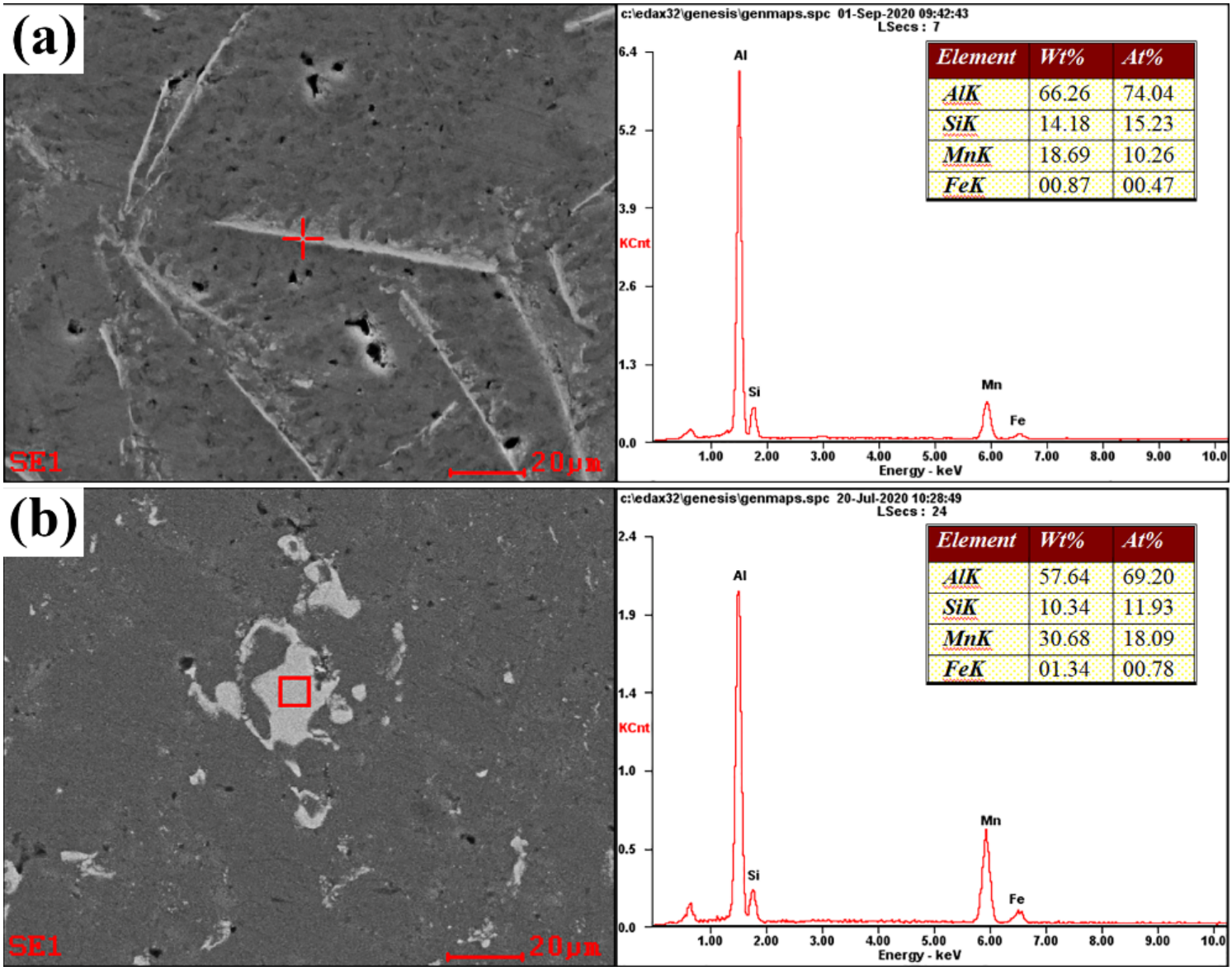

Figure 5

SEM-EDS analysis results of the Al-12Si-1.0Mn-0.6Mg-0.1Sc (a) and the Al-12Si-1.0Mn-0.6Mg-0.3Sc alloys (b) Note: The designations employed and the presentation of the material on this map do not imply the expression of any opinion whatsoever on the part of Research Square concerning the legal status of any country, territory, city or area or of its authorities, or concerning the delimitation of its frontiers or boundaries. This map has been provided by the authors.

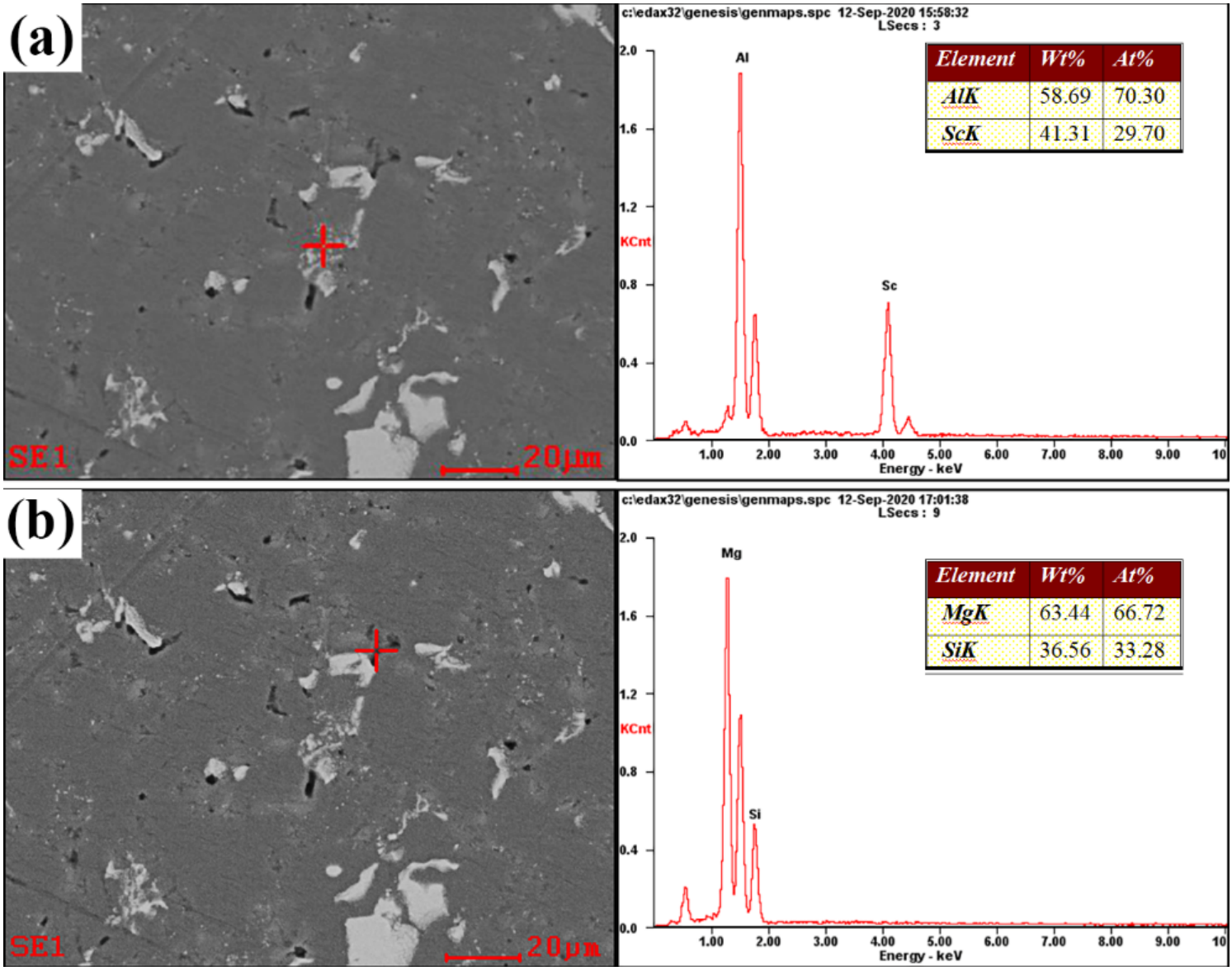

Figure 6

SEM-EDS analysis results of the Al-12Si-1.0Mn-0.6Mg-0.3Sc alloy Note: The designations employed and the presentation of the material on this map do not imply the expression of any opinion whatsoever on the part of Research Square concerning the legal status of any country, territory, city or area or of its authorities, or concerning the delimitation of its frontiers or boundaries. This map has been provided by the authors.

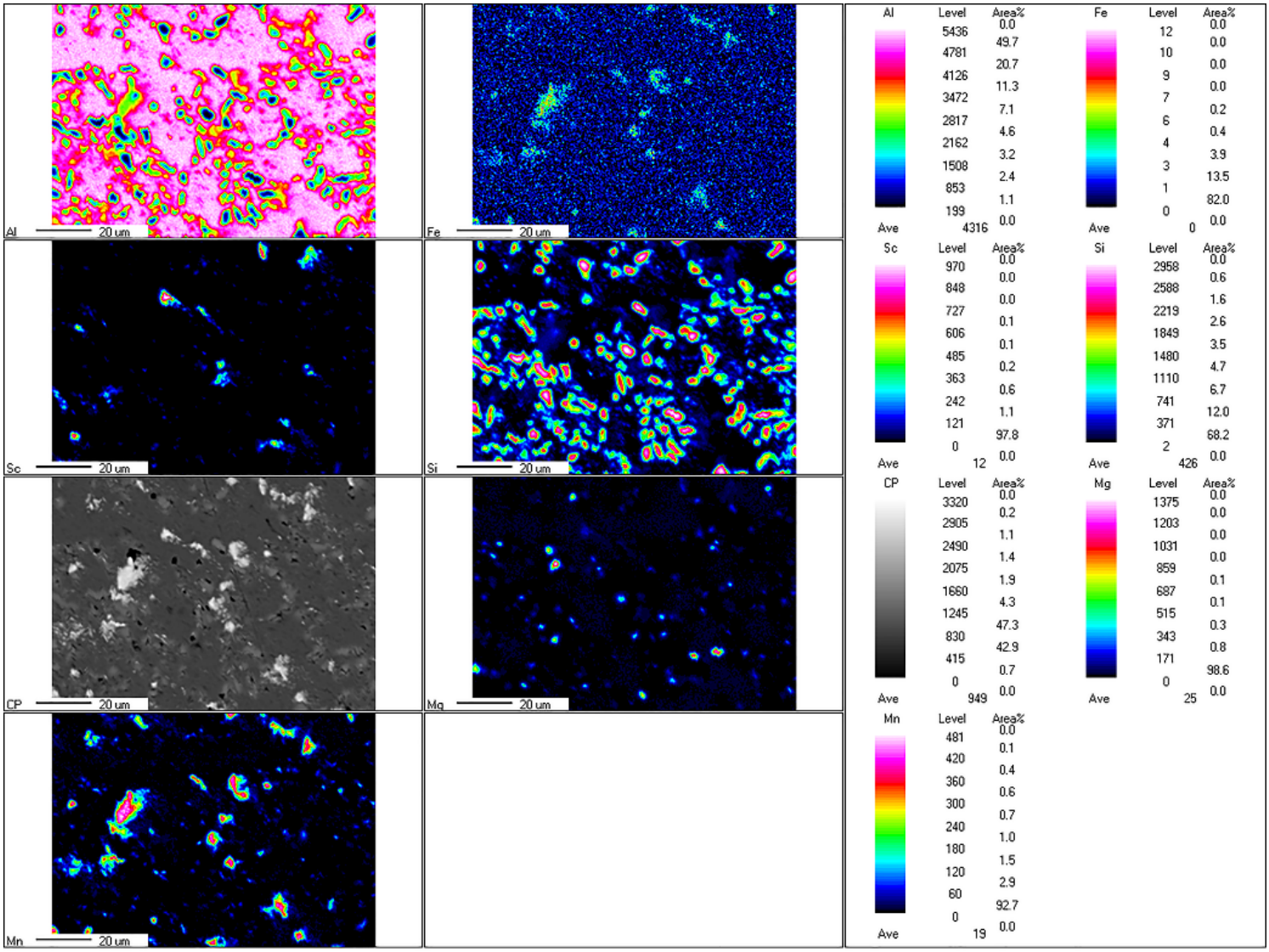

Figure 7

EPMA distribution diagram of Al-12Si-1.0Mn-0.6Mg-0.3Sc alloy

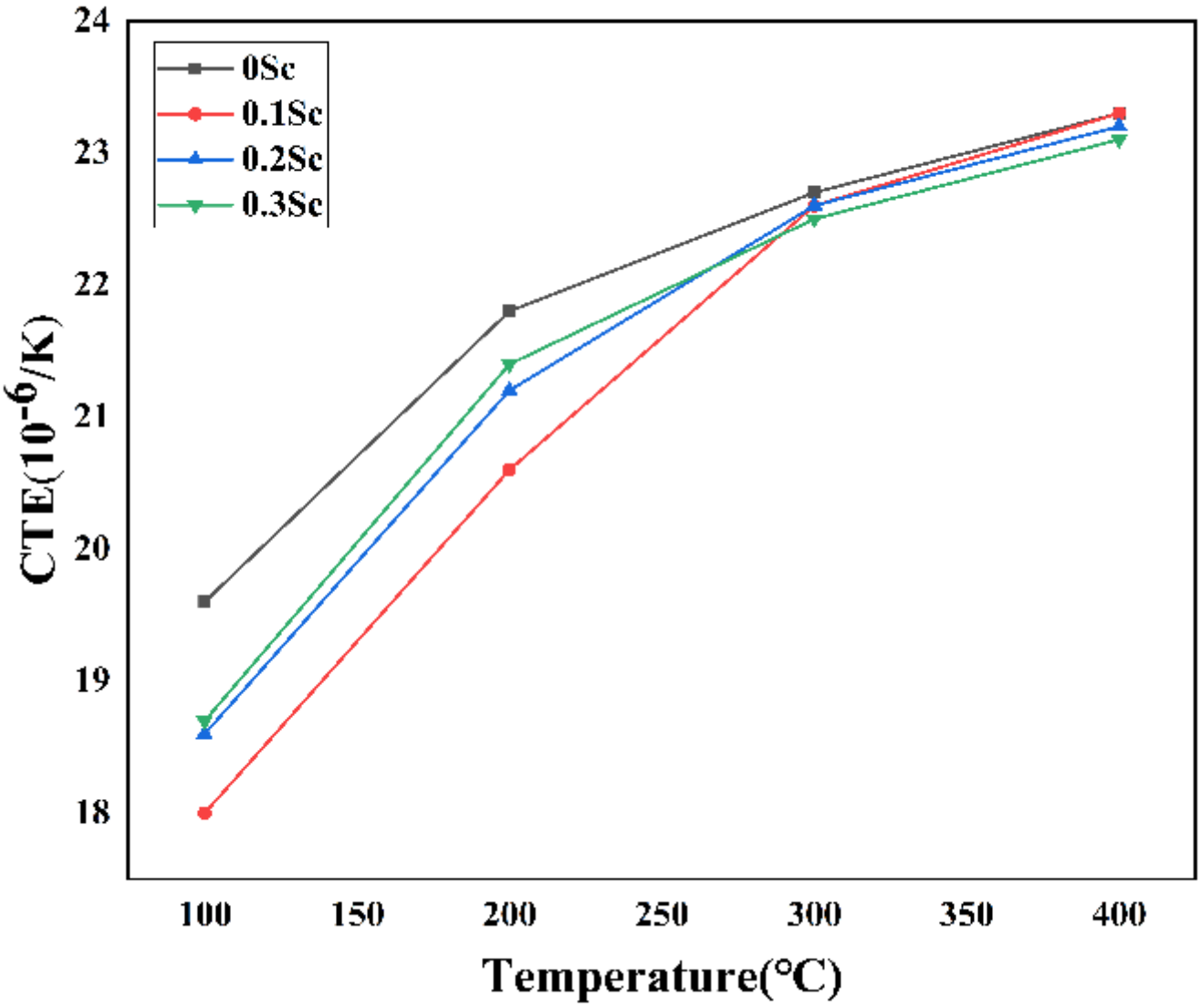

Figure 8

The relationship between thermal expansion coefficient and temperature of the Al-12Si-1.0Mn-0.6Mg-xSc (x = 0, 0.1, 0.2, and 0.3) alloys

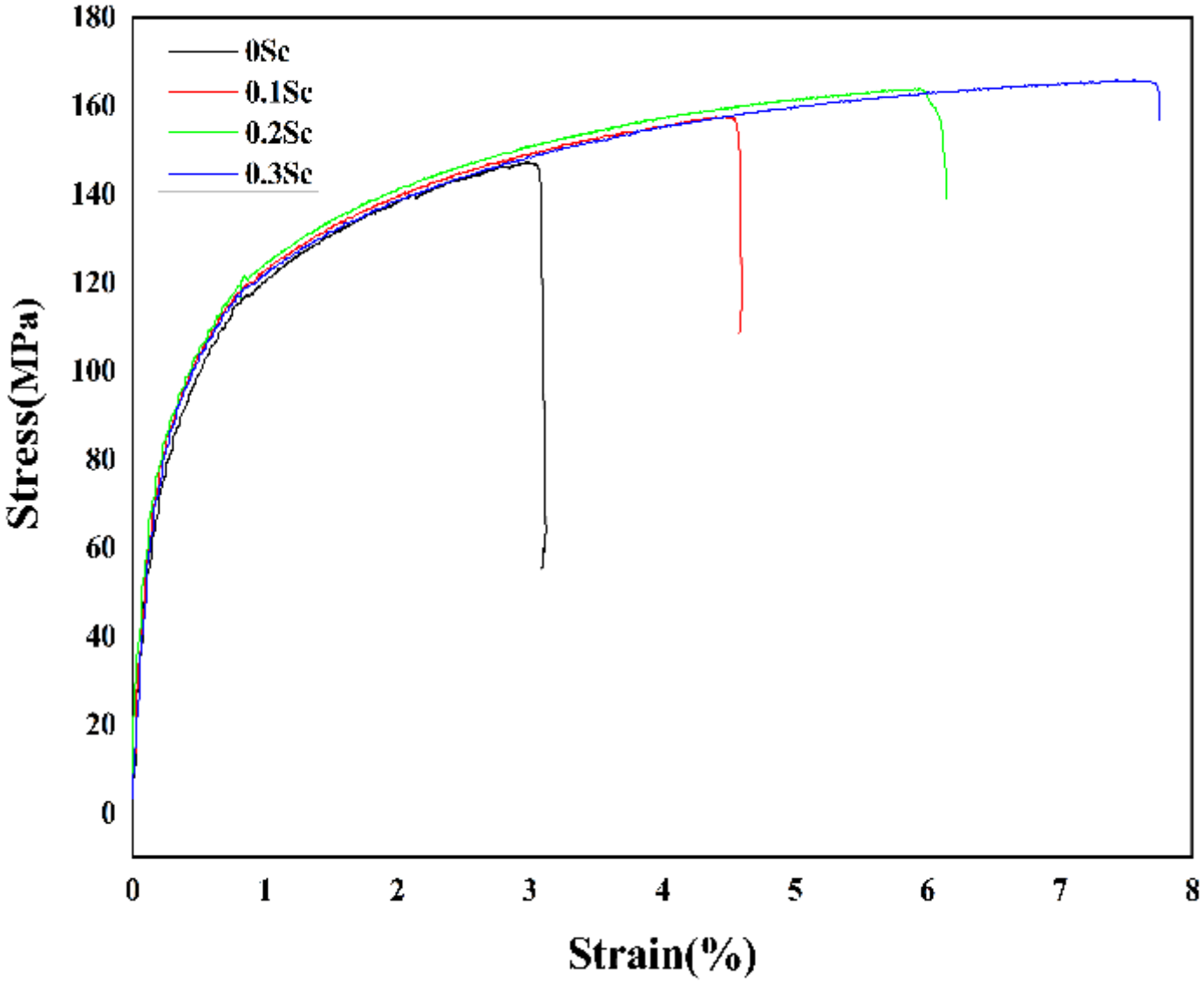

Figure 9

Tensile stress-strain behavior of the Al-12Si-1.0Mn-0.6Mg-xSc (x = 0, 0.1, 0.2, and 0.3) alloys

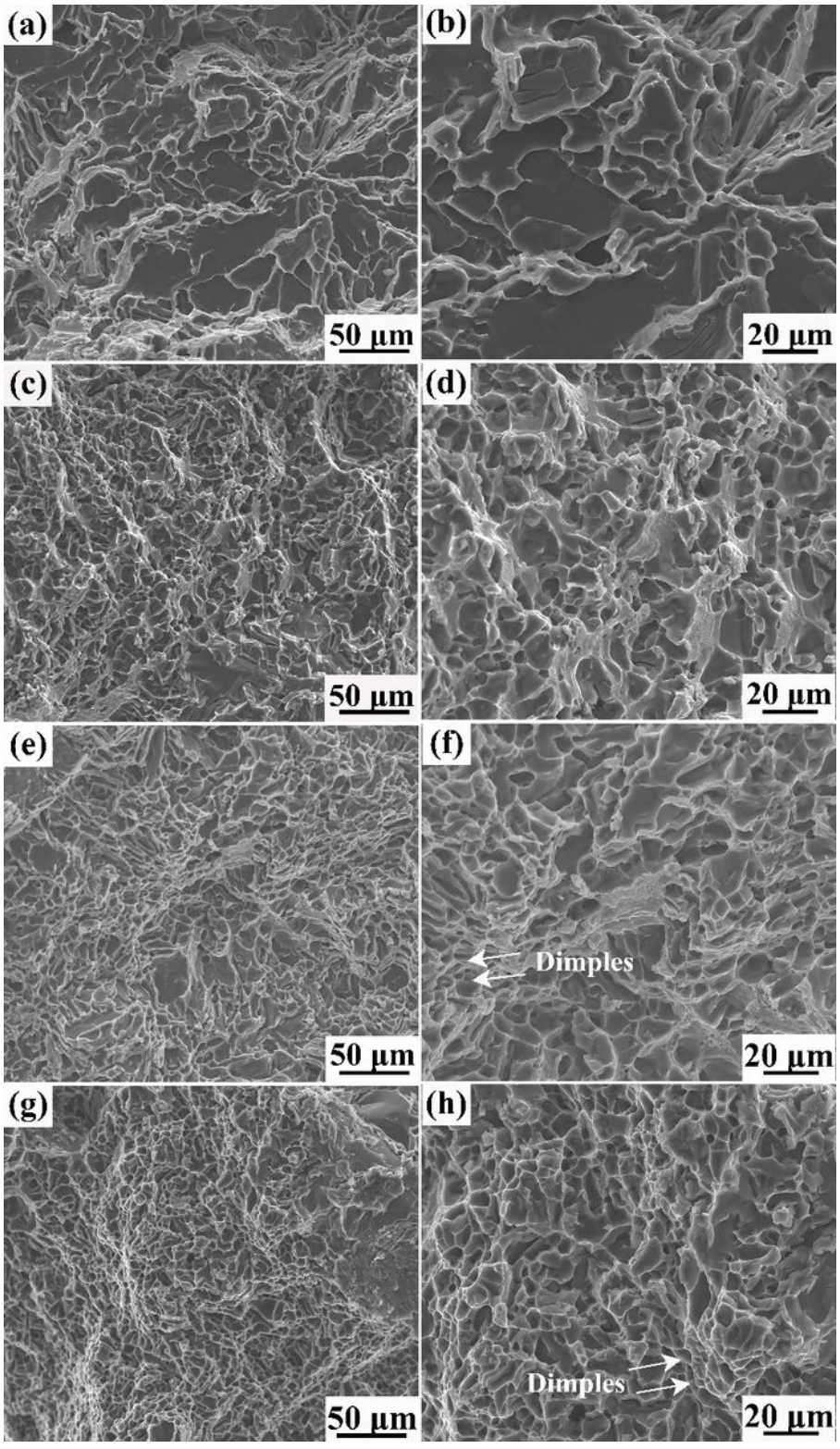

Figure 10

Fracture morphologies of the Al-12Si-1.0Mn-0.6Mg-xSc (x = 0, 0.1, 0.2, and 0.3) alloys

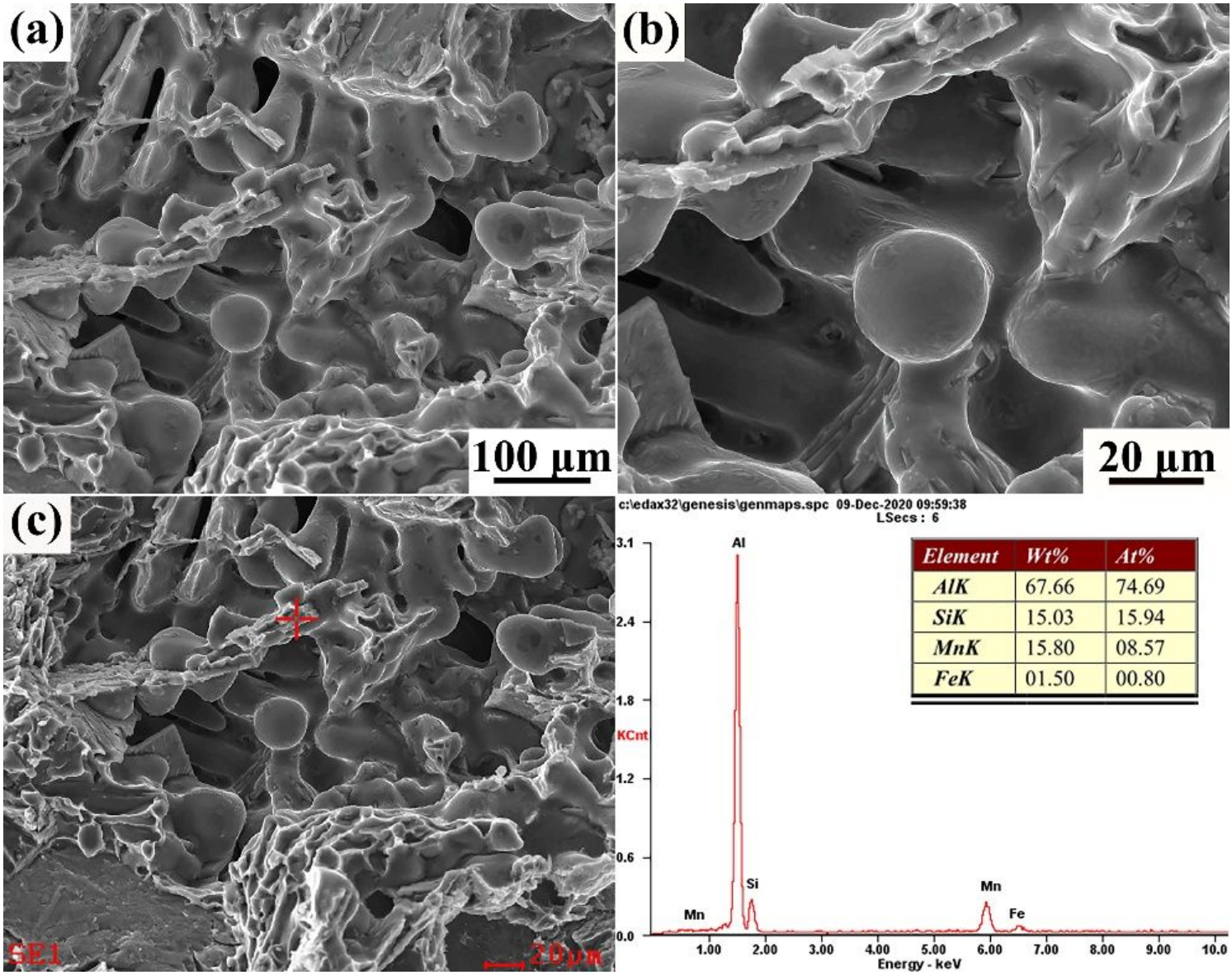

Figure 11

Shrinkage cavity on fracture surface of the Al-12Si-1.0Mn-0.6Mg alloy 3.4 Corrosion resistance

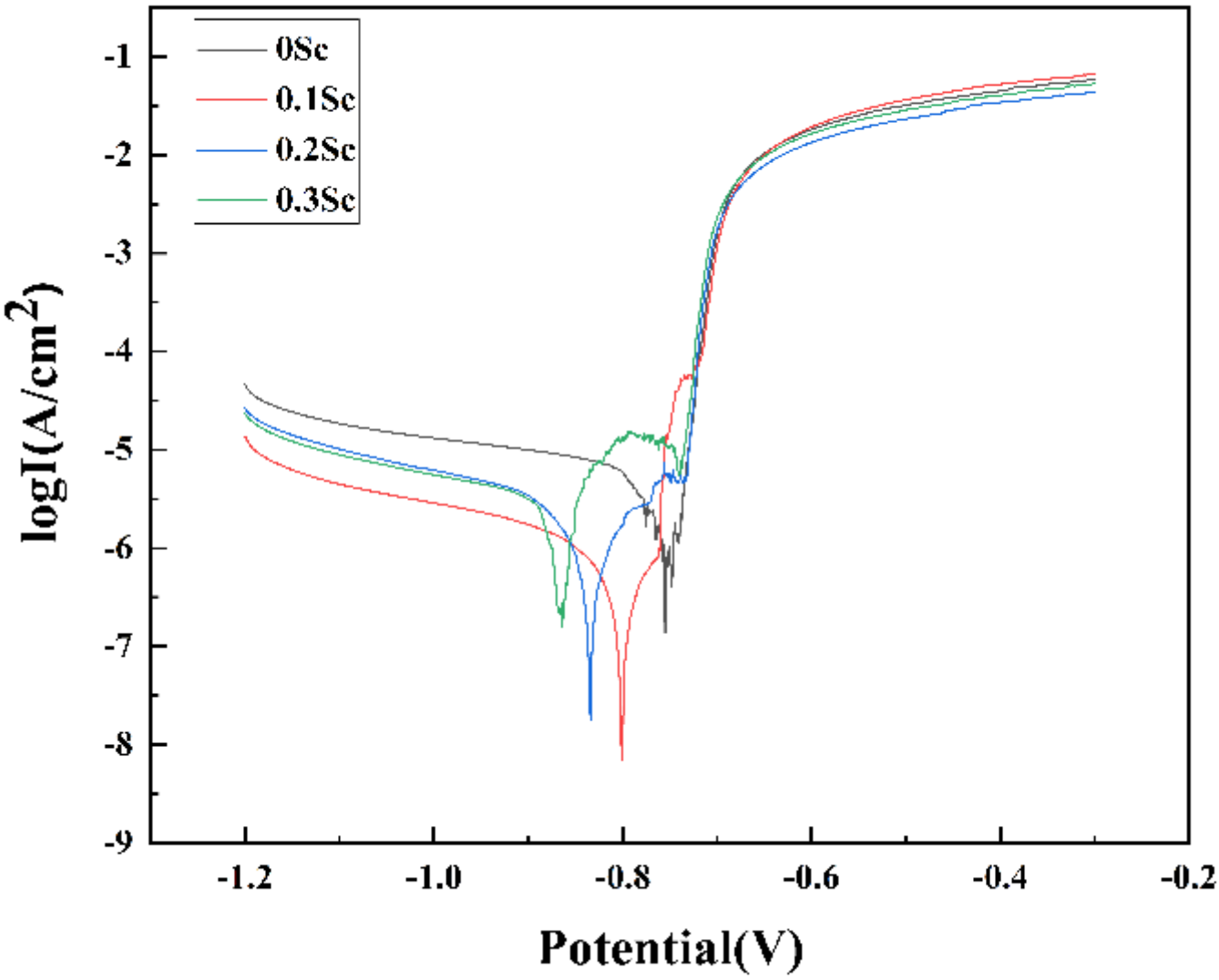

Figure 12

Dynamic potential polarization curves of the Al-12Si-1.0Mn-0.6Mg-xSc (x = 0, 0.1, 0.2, and 0.3) alloys